Cytometry
PART A
Journal of the International Society for Advancement of Cytometry

Image Analysis of Neural Stem Cell Division Patterns in the Zebrafish Brain

Valerio Lupperger,[1] Felix Buggenthin,[1] Prisca Chapouton,[2]* Carsten Marr[1]*

[1]Institute of Computational Biology, Helmholtz Zentrum München - German Research Center for Environmental Health, Ingolstädter Landstr. 1, 85764 Neuherberg, Germany

[2]Research Unit Sensory Biology and Organogenesis, Helmholtz Zentrum München - German Research Center for Environmental Health, Ingolstädter Landstr. 1, 85764 Neuherberg, Germany

Received 30 May 2016; Revised 30 August 2017; Accepted 6 September 2017

*Correspondence to: Carsten Marr; Institute of Computational Biology, Helmholtz Zentrum München - German Research Center for Environmental Health, Ingolstädter Landstr. 1, 85764 Neuherberg, Germany. E-mail: carsten.marr@helmholtz-muenchen.de or Prisca Chapouton; Research Unit Sensory Biology and Organogenesis, Helmholtz Zentrum München - German Research Center for Environmental Health, Ingolstädter Landstr. 1, 85764 Neuherberg, Germany. E-mail: chapouton@helmholtz-muenchen.de

Published online 00 Month 2017 in Wiley Online Library (wileyonlinelibrary.com)

DOI: 10.1002/cyto.a.23260

© 2017 International Society for Advancement of Cytometry

• **Abstract**

Proliferating stem cells in the adult body are the source of constant regeneration. In the brain, neural stem cells (NSCs) divide to maintain the stem cell population and generate neural progenitor cells that eventually replenish mature neurons and glial cells. How much spatial coordination of NSC division and differentiation is present in a functional brain is an open question. To quantify the patterns of stem cell divisions, one has to (i) identify the pool of NSCs that have the ability to divide, (ii) determine NSCs that divide within a given time window, and (iii) analyze the degree of spatial coordination. Here, we present a bioimage informatics pipeline that automatically identifies GFP expressing NSCs in three-dimensional image stacks of zebrafish brain from whole-mount preparations. We exploit the fact that NSCs in the zebrafish hemispheres are located on a two-dimensional surface and identify between 1,500 and 2,500 NSCs in six brain hemispheres. We then determine the position of dividing NSCs in the hemisphere by EdU incorporation into cells undergoing S-phase and calculate all pairwise NSC distances with three alternative metrics. Finally, we fit a probabilistic model to the observed spatial patterns that accounts for the non-homogeneous distribution of NSCs. We find a weak positive coordination between dividing NSCs irrespective of the metric and conclude that neither strong inhibitory nor strong attractive signals drive NSC divisions in the adult zebrafish brain. © 2017 International Society for Advancement of Cytometry

• **Key terms**

bioimage informatics; neural stem cells; zebrafish brain; cell identification; neuroscience image computing

THE analysis of spatial patterns is prevalent in distinct disciplines such as ecology (1,2), geostatistics (3), and developmental biology (4). Adult neural stem cells (NSCs) have been found at specific locations within the brain of adult vertebrates [reviewed in (5,6)], but the spatiotemporal regulation of NSC quiescence and proliferation is only roughly understood. To investigate dividing NSCs and the maintenance of stem cell pools, the zebrafish is an ideal model organism due to its high neurogenic activity, its accessibility for imaging, and the availability of transgenic lines.

In the adult zebrafish pallium (the dorsal telencephalon, see Fig. 1), the ventricular zone containing the NSCs is located on the surface, as a result of an eversion during development (7). The dorsal domain is a spatially clearly defined two-dimensional (2D) surface at the border of the telencephalon. NSCs within this surface repopulate mature neurons and glial cells via constant proliferation and differentiation (8,9). This situation has been utilized in in vivo imaging studies to follow the fate of labeled NSCs (10,11) over several weeks. To describe the spatial organization of all cycling NSCs within the pool of NSCs, we used whole mount preparations and labeled S-phase NSCs within three-dimensional (3D) images of the ventricular zone.

ISAC
International Society for Advancement of Cytometry

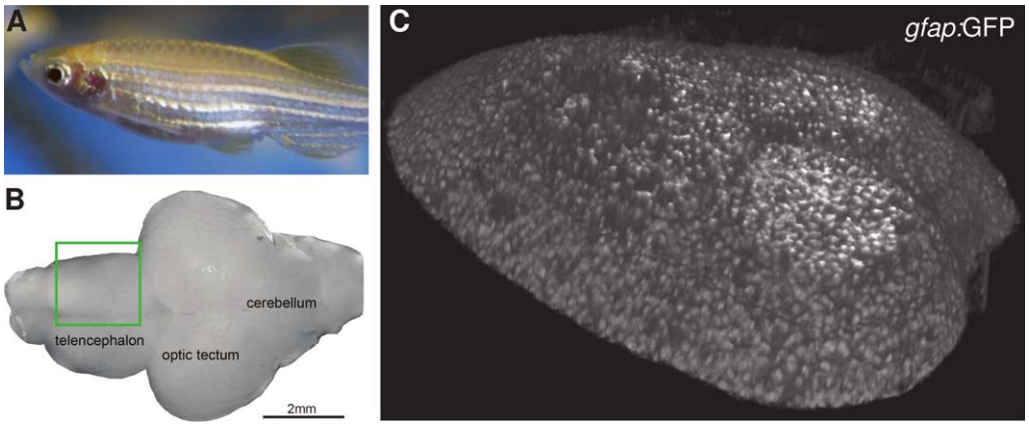

Figure 1. NSCs in the zebrafish telencephalon. (**A**) In all experiments, four-month-old zebrafish of a *gfap*:GFP transgenic strain were used, where green fluorescent protein (GFP) is expressed under the control of *gfap* enhancer elements. Average length of adult fish is ∼3 cm (**B**) Top view on a zebrafish brain showing the telencephalon, optic tectum, and cerebellum. We image one hemisphere of the telencephalon (marked with a green rectangle). Scale bar: 2 mm. (**C**) Reconstructed 3D image stack from confocal microscopy. [Color figure can be viewed at wileyonlinelibrary.com]

Identification and segmentation of single cells in 3D image stacks is a challenging problem for quantitative bioimaging. To identify single nuclei in 3D, several methods were recently proposed (12–17) that rely on nuclear staining. Such automated methods normally start with separation of background and foreground, followed by the identification of single objects, using, for example, k-means (12), water shedding (13), or graph-cut segmentation (14). Notably, the application of available methods to a specific data set requires adaptation and manual fine-tuning of the parameters. For neural neuronal cells, Schmitz et al. (18) recently stated that available methods fail to properly identify single cells in 3D.

Here, we present a single-cell identification pipeline (SCIP) that explicitly uses prior knowledge on the organization of NSCs in the zebrafish brain. It exploits the fact that NSCs in the zebrafish brain are located on a 2D surface to accurately identify them in 3D. A polynomial regression model as approximation to the hemisphere surface improves the identification and is used to remove imaging artifacts. We apply SCIP to six 3D image stacks of adult zebrafish hemispheres, automatically identify thousands of NSCs, and apply three different metrics to determine distances between all pairs of cells. Within the six hemispheres, we then locate stem cells in S-Phase labeled by the incorporated thymidine analogue EdU. To assess a possible interaction between the dividing cells quantitatively, we evaluate and later fit a simple interaction model and find a weak positive coordination of S-Phase NSCs.

Materials and Methods

Animal Maintenance

Zebrafish (*Danio rerio*) were kept in the fish facility of the Helmholtz Zentrum München at 28°C with a light/dark cycle of 14/10 h. We used four-month old zebrafish (Fig. 1A) of the transgenic line *gfap*:GFP (19) in an AB background. Experiments were performed in accordance with the regulations of the Regierung von Oberbayern on animal welfare (Animal protocol 55.2-1-54-2531-83-14).

Sample Preparation and Image Acquisition

In the transgenic *gfap*:GFP zebrafish strain (19) NSCs are fluorescently labeled with GFP under the control of *gfap* enhancer. Dividing cells were labeled by intraperitoneal injection of the thymidine analogue 5-ethynyl-2-deoxyuridine (EdU, 1 mg/ml, 5 μl/0.1 g body weight), which incorporates into replicating DNA, one hour before killing the animals and brain fixation. Zebrafish were over-anesthetized and killed in 0.1% buffered MS222, the brains dissected and fixed overnight in 4% PFA. After blocking in 10% normal goat serum (Sigma), EdU was revealed by binding to azide-Alexa Fluor 555 through a click reaction (Invitrogen). Brains were mounted in Vectashield medium (Vector Laboratories) between two coverslips separated by parafilm spacers.

An inverted confocal laser scanning microscope (Leica SP5) with a 20× glycerol immersion objective (HC PL APO 20×/0.70 IMM CS), which corrects for field curvature astigmatism, was used for image acquisition. The field of view covers one hemisphere of the pallium (dorsal telencephalon) nearly completely (see Figs. 1B and 1C). All images were taken with 2048 × 2048 pixel in x-y direction with a pixel size of 0.38 × 0.38 μm. Resolution in z direction differed between the 6 hemispheres (Experiment 1: 49 and 62 slices with distance of 2.0 μm, Experiment 2: 72 and 84 slices with distance of 2.2 μm, Experiment 3: 105 and 85 slices with distance of 1.3 μm) and was adapted to brain size. Visual inspection confirms that aberration effects are minimal and do not impinge on cell identification.

Single-Cell Identification Pipeline

Starting from a 3D image stack (Fig. 2A) SCIP projects the maximum intensity of every x-y coordinate in z-direction to a 2D image (Fig. 2B). A Laplace of Gaussian (LoG) filter followed by a local maximum/minimum search is used to identify cell sized blobs of approximately $b = 8$ μm in

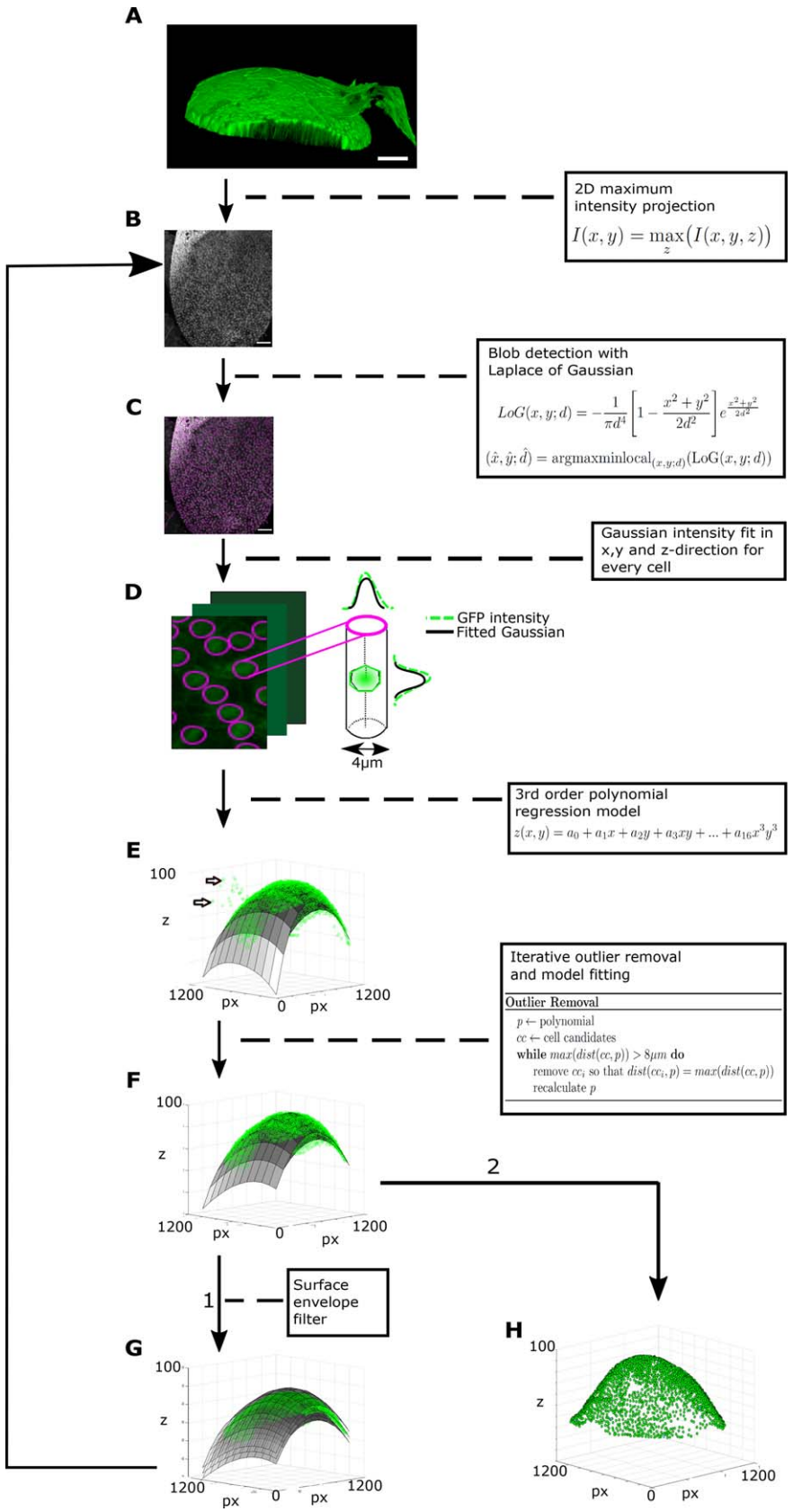
A
2D maximum intensity projection
$I(x,y) = \max_z(I(x,y,z))$
B
Blob detection with Laplace of Gaussian
$LoG(x,y;d) = -\frac{1}{\pi d^4}\left[1 - \frac{x^2+y^2}{2d^2}\right] e^{\frac{x^2+y^2}{2d^2}}$
$(\hat{x},\hat{y};\hat{d}) = \text{argmaxminlocal}_{(x,y;d)}(\text{LoG}(x,y;d))$
C
Gaussian intensity fit in x,y and z-direction for every cell
D
GFP intensity
Fitted Gaussian
4µm
3rd order polynomial regression model
$z(x,y) = a_0 + a_1x + a_2y + a_3xy + ... + a_{16}x^3y^3$
E
100
z
1200
px
0
px
1200
Iterative outlier removal and model fitting
Outlier Removal
$p \leftarrow$ polynomial
$cc \leftarrow$ cell candidates
while $max(dist(cc,p)) > 8\mu m$ do
remove cc_i so that $dist(cc_i,p) = max(dist(cc,p))$
recalculate p
F
2
1
Surface envelope filter
G
H

Figure 2.

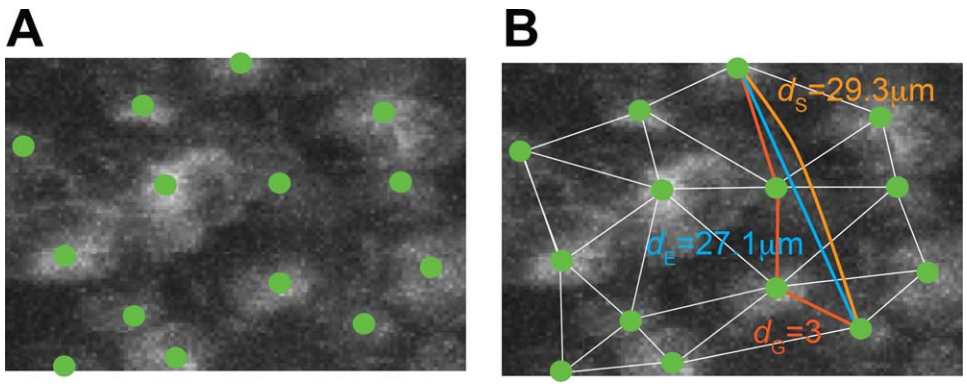

Figure 3. Three metrics are defined on the hemispheres. NSCs are identified (**A**) and then used to calculate the Euclidean distance d_E (blue line), the surface distance d_S (orange line) and the graph distance d_G (red lines) between all pairs of identified cells on the 2D surface (**B**). For the surface distance, the shortest path between two cells in 3D is projected on the surface fitted with SCIP. For the graph distance, the shortest path in a network derived from a Delaunay triangulation is calculated. Identified NSCs are shown in green on top of the *gfap*:GFP signal. [Color figure can be viewed at wileyonlinelibrary.com]

diameter as possible cell candidates (Fig. 2C). From every detected blob, the *x*-*y* centroid is used for the determination of the *z*-coordinate. To discard possible signals from neighboring cells, we use pixel information inside a cylinder with a diameter of 4 μm around the centroids (Fig. 2D) and fit a Gaussian curve to the mean intensity profile along *z*. This allows to filter out false positives due to contaminations during sample preparation. The argument of the maximum (arg max) of the fitted Gaussian is used as the *z*-coordinate of the cell centroid. Additionally, its standard deviation is used to filter real cells from image artifacts: Single pixel errors show a strong intensity and a small standard deviation. We thus filter out objects with a standard deviation in *z* below 1.5 μm. Analogously, a 2D Gaussian distribution is fitted in *x*-*y* direction and objects with a standard deviation below 2 μm are excluded.

As NSCs are only found on the edge of a hemisphere we fit a third order polynomial to all 3D centroids to roughly approximate the hemisphere surface and avoid overfitting of single cells. The fitted model is used to exclude outliers by repetitively removing the most distant cell candidate (see arrows in Fig. 2E) and recalculating the polynomial model. The procedure is repeated until all cells are closer than 16 μm (~two cell diameters) to the polynomial surface (Fig. 2F).

As cells from the adjacent hemisphere, and image contaminations from the 3D image stack may overlap with real cells in the 2D projection, we introduce an envelope in *z*-direction 20 μm above and below the polynomial (Fig. 2G). All pixels outside this envelope are set to background intensity, determined via the median of the eight corner pixels of the 3D stack. Steps (B) - (F) of the pipeline are then repeated on the filtered image stack. The resulting 3D centroids (Fig. 2H) represent NSCs on the zebrafish hemisphere and are used for further analyses.

Distance Measures

We define distances between pairs of cells using three metrics (Fig. 3): (i) The Euclidean distance d_E between two points in the 3D space in μm. (ii) The surface distance d_S is the projection of the shortest path between two cells on the polynomial in μm. (iii) The graph distance d_G between two cells is the number of edges connecting the cells in the shortest path of a graph consisting of nodes (the NSCs identified) and edges between them (see Fig. 3B) as calculated with a Delaunay triangulation (20). The shortest path is determined using the Floyd-Warshall algorithm (21,22).

Identification of S-Phase NSCs

We gave a pulse of EdU 1 h prior to brain dissection, fixation, fluorescent staining and imaging. Cells with a fluorescent EdU signal (see Fig. 4) were automatically identified with SCIP. For optimal data quality, we manually verified S-phase NSCs as EdU positive cells that are also positive for *gfap*:GFP.

Influence Model

From the observed patterns of S-phase NSCs (Fig. 4), we ask whether specific rules underlie the spatial arrangement of division events. To quantify the distribution of S-phase NSCs within the set of all NSCs, we introduce P_i, the probability that an NSC *i* is in S-phase at a particular time point, as a function of S-phase NSCs in the neighborhood of cell *i*. In the case of no influence between division events, this probability is the same for all NSCs. To simulate a pattern with *S* S-phase

Figure 2. SCIP for NSCs in the adult zebrafish brain. Raw 3D data (**A**) is transformed into 2D images (**B**) via 2D maximum intensity projection. Cell somata are touching each other on the surface, without intermediate space. Cell centers display a high GFP intensity and are used for identification. A blob detection using LoG identifies cell candidates (**C**). A Gaussian curve is fitted to the intensity profile of a cylinder with 4 µm diameter along *z* of every cell candidate (**D**). The mean of the Gaussian is taken as the *z*-coordinate of cell candidate centroid. A surface based on a 3rd order polynomial regression model is fitted to all centroids (**E**). Cells that are further away than two cell diameters (~16 µm) are excluded step by step by removing iteratively the most distant outlier and recalculate the surface (**F**). To remove remaining image artifacts an envelope is placed in 20 µm distance around the surface (**G**). All pixels outside this envelope are set to background intensity. Afterwards the pipeline starts over again at (B) using the filtered image stack without image artifacts. (**H**) The resulting cell centroids can now be used for further analyses. Scale bars: 50 µm. [Color figure can be viewed at wileyonlinelibrary.com]

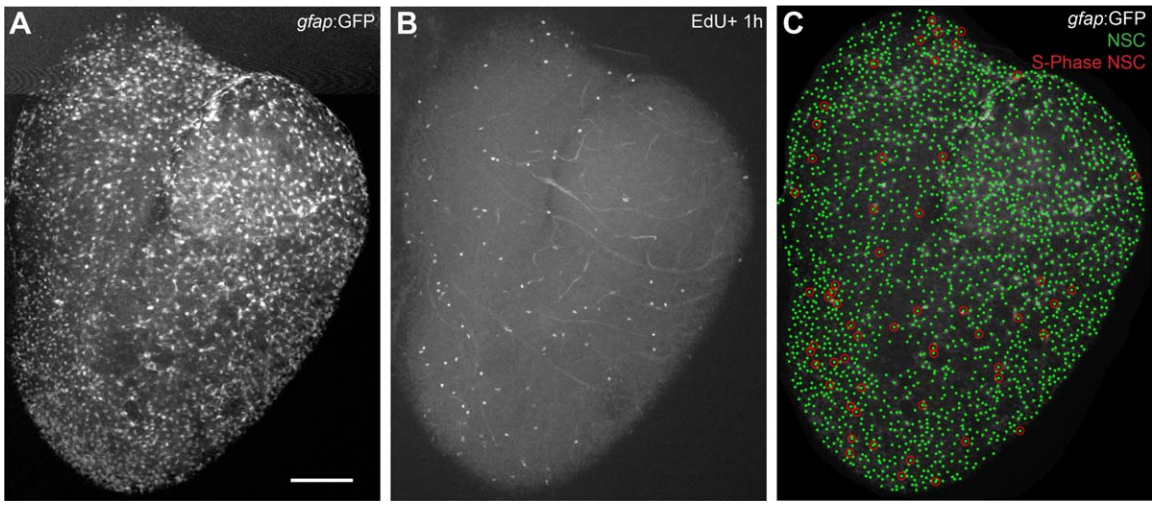

Figure 4. Spatial pattern of NSC divisions. NSCs are identified in the gfap:GFP channel (**A**) using SCIP. Cells in S-phase were automatically identified by EdU signal and manually verified (**B**). S-phase NSCs are identified as cells that appear both in the gfap:GFP and in the EdU channel (**C**). Scale bar: 100 μm. [Color figure can be viewed at wileyonlinelibrary.com]

NSCs, we randomly select S cells from all N NSCs, where the probability for NSC i to be selected, P_i, can be normalized to

$$p_i = 1/N. \quad (1)$$

To account for an attractive or repulsive influence between S-phase NSCs, we scale this probability with a positive parameter g. The exponent of g is the number of S-phase NSCs within a distance r (Fig. 5). The probability P_i for cell i to be selected as an S-phase NSC then becomes

$$P_i = g^{\sum_{j=1,j\neq i}^{S} I(\mathrm{dist}(i,j)\leq r)}/Z \quad (2)$$

where we evaluate the number of S-Phase NSCs within radius r using the indicator function I, and

$$Z = \sum_{k=1}^{N} g^{\sum_{j=1,j\neq k}^{S} I(\mathrm{dist}(k,j)\leq r)}$$

is the normalization constant. To simulate a pattern with S S-phase NSCs, we now select S cells one after the other and update the probabilities P_i after each selection.

Without any influence between S-phase NSCs, $g = 1$ and Eq. (2) simplifies to Eq. (1). For $g < 1$ or $g > 1$ we induce a repulsive or attractive influence within a distance r, leading to visually distinct patterns of S-phase NSCs (Fig. 5).

Parameter Inference

From the division probability [Eq. (2)], we can calculate the likelihood L for an observed S-phase pattern given the interaction strength g and interaction radius r. The log-likelihood for S cells in S-Phase within the set of N NSCs is

$$\log L(g,r) = \sum_{i=1}^{S} \log P_i. \quad (3)$$

We can calculate the sum of log-likelihoods for all observed brain hemispheres and find the maximum likelihood estimate for our parameters g and r by optimizing Eq. (3): First, we evaluated all combinations of g and r with $g \in \{0.1, 0.2, \ldots, 4\}$ and $r \in \{5, 6, \ldots, 150\}$ μm for Euclidean distance d_E and surface distance d_S, and $r \in \{1, 2, \ldots, 20\}$ cells for graph distance d_G, respectively. From the parameter combination with the largest L, we then start a gradient descent optimization algorithm (using MATLAB'S Fmincon function).

To evaluate our inference algorithm, we repeatedly generated 30 data sets per tested influence parameter combination with different influence strengths and radii and applied our inference algorithm to them (see Fig. 6). In the box plots, the boundary of the box closest to zero indicates the 25th percentile ($q1$), a black line within the box marks the median, and the boundary of the box farthest from zero indicates the 75th percentile ($q3$). Whiskers above and below the box include points that are not outliers. Points are considered as outliers if they are bigger than $q3 + 1.5(q3 - q1)$ or smaller than $q1 - 1.5(q3 - q1)$.

Implementation

SCIP and the statistical analysis are implemented in MATLAB and performed on a Windows 7 machine with 4 cores (i7–5500 U, 2.4 GHz) and 16 Gigabyte DDR3 memory. The time to identify NSCs in one hemisphere took between 5

Table 1. Evaluation of three NSC identification methods

	SCIP	3D OBJECT COUNTER	IMARIS
Precision	**93 ± 3%**	91 ± 5%	92 ± 4%
Recall	**91 ± 6%**	66 ± 14%	**91 ± 3%**
F_1 score	**92 ± 2%**	76 ± 9%	91 ± 1%

NSCs have been counted manually (by P.C.) in 5 different regions in the 2D maximum intensity projection of three zebrafish hemispheres (see Fig. 7). We show precision, recall, and F_1 score (mean ± s.d., $n = 5$ regions) for SCIP, the 3D object counter plugin in ImageJ, and Imaris. Best mean values are indicated in bold.

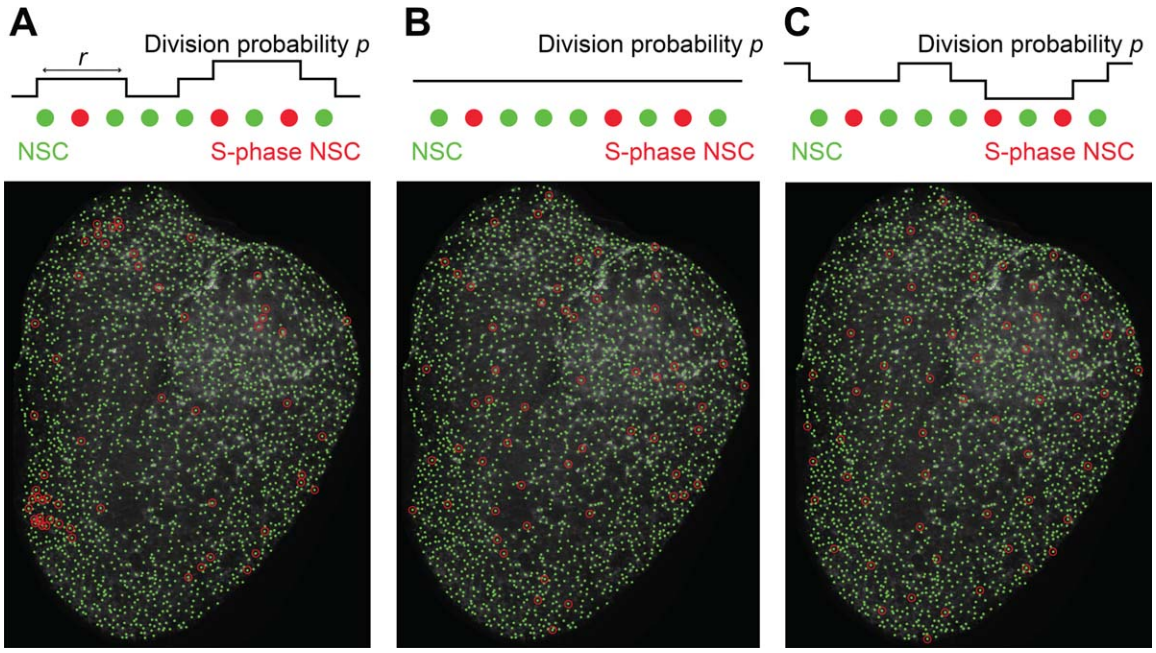

Figure 5. Simulated attractive spatial influence (**A**), no spatial influence (**B**), and repulsive spatial influence (**C**) of S-phase NSCs result in visually distinct patterns. [Color figure can be viewed at wileyonlinelibrary.com]

and 10 min. Parameter estimation for one hemisphere took between 3 and 8 min. Code available at https://github.com/QSCD/SCIP.

Results

Identification of Neural Stem Cells Using SCIP

SCIP can be used to identify single NSCs on the 2D hemisphere surface. We evaluate the quality of cell identification via SCIP by comparing automatically derived cell counts of NSCs in the 2D maximum intensity projection in five different regions of three hemispheres to those generated manually by a human expert on a 2D maximum intensity projection (exemplarily shown as green circles in Fig. 7). We manually count 94, 84, 118, 136, and 160 cells in the five regions. SCIP identifies 85, 92, 123, 125, and 151 NSCs in the same five regions. Pairs of manual ("true") and automatically identified NSCs were matched according to their *x-y* coordinate, which allowed us to calculate precision (the fraction of true NSCs within the set of NSCs identified by SCIP, Fig. 7A), recall (the fraction of NSCs identified by SCIP within all true NSCs) and the F_1 score [an accuracy measure that considers both precision and recall (23)]. We compare SCIP to two other standard approaches for cell identification and segmentation: The "3D object counter" plugin (24) in ImageJ (25) where we carefully chose the intensity threshold as 75 to optimally match our manual counts, and the commercial Imaris software (version 8.4.1, Bitplane, Zurich, Switzerland; Fig. 7C), with target cell diameter of 5 μm and an intensity threshold of 7.14.

The 3D object counter identifies only a fraction of the manually annotated cells (recall 66 ± 14%, mean ± s.d., $n = 5$ regions). Cells that are close to each other are often identified as large single objects. SCIP and Imaris were able to identify NSCs with the same recall but SCIP identifies less false positive cells resulting in a slightly higher precision and F_1 score compared to Imaris (see Table 1). Overall, we expect that the manual counts underestimate the number of NSCs slightly due to the inherent unidentifiability of nearby cells with a small shift in *z* direction in the 2D maximum intensity projection.

NSC Divisions in the Zebrafish Brain

We apply SCIP to six zebrafish hemispheres from three different adult animals. In each hemisphere, we automatically identify NSCs using SCIP. Moreover, we identify S-phase NSCs via a fluorescently labeled EdU incorporation 1 h prior to imaging (see Methods), stained in a second fluorescence channel (Fig. 4).

In six hemispheres, we identify between 1458 and 3195 NSCs (Table 2). Furthermore, we identify between 42 and 67 S-phase NSCs. The ventricular zone contains dividing NSCs [called type II progenitors (8,26)] as well as type III dividing progenitors that do not express *gfap*:GFP. We consider in this study specifically the dividing type II NSCs. The fraction of S-phase NSCs is 2.6% ± 0.9% (mean ± s.d., $n = 6$ hemispheres). This fraction is low compared to values obtained with PCNA and MCM5 cell cycle markers (11,26) due to EdU labeling of S-phase only within the small time window of one hour. Visually, the S-phase NSCs (marked by red circles in Fig. 4C) form no obvious cluster, but regions in the brain that show a depletion of S-phase NSCs seem to appear.

Analysis of S-Phase Patterns

To quantify a potential spatial attraction or repulsion of S-phase NSCs, we define a probabilistic spatial model, where

Table 2. We identify around 2.5% of S-phase NSCs in each of the six hemispheres

HEMISPHERE ID	NSCS	S-PHASE NSCS	FRACTION OF S-PHASE NSCS
Exp1L	2399	67	2.79%
Exp1R	2046	56	2.74%
Exp2L	3195	46	1.44%
Exp2R	3017	56	1.86%
Exp3L	1458	56	3.84%
Exp3R	1482	42	2.83%

NSCs have been automatically identified using SCIP, S-phase NSCs have been additionally manually verified.

the division probability of NSCs is regulated by two parameters: an interaction radius r, and the strength g of the interaction within this radius r. For $g = 1$, the probability to enter S-phase is not changed, but it is increased or decreased for g above or below 1, respectively (see Fig. 5 and Methods). We simulate patterns of S-phase NSCs (same number as observed) for an attractive (with $r = 50$ μm and $g = 1.6$), no influence ($g = 1$), and repulsive ($r = 50$ μm and $g = 0.1$, see Fig. 5) model. Visually, the three different models can be discriminated clearly via clustering of events (Fig. 5A), spatially random events (Fig. 5B), and events that are evenly spaced across the surface (Fig. 5C).

Formulating the likelihood of the observed spatial pattern of S-phase NSCs [Eq. (3)] allows to infer the most likely parameters r and g for the assumed probabilistic model. For simulated data, both parameters are inferred reliably for realistic range of parameters (Fig. 6). Here, we simulated patterns by drawing the same number of S-phase NSCs as observed in the data one after the other, consecutively updating the probabilities P_i for the next draw based on the chosen parameters g and r. We determine the maximum likelihood estimate for the two parameters by maximizing the log-likelihood, which sums over all six hemispheres.

We finally apply our inference algorithm to the S-Phase NSC patterns in the six hemispheres (see Table 2 and Fig. 4). Using the surface distance d_S, we identify the most likely model with a weak positive influence ($g = 1.15$) between S-phase NSCs and an interaction radius of 100 μm. The most likely model for the Euclidean distance d_E has an interaction radius of 89 μm with a weak positive influence ($g = 1.16$). Since the surface and Euclidean distances are ignorant of the inhomogeneous density of NSCs on the brain, we also infer the parameters of our probabilistic model for the graph distance d_G. Here we identify again a weak positive influence ($g = 1.17$) to be most consistent with the observed data with an influence radius of 6 cells (Table 3). Correlating graph distance d_G with surface distance d_S on the six hemispheres, we find that a $d_G = 6$ corresponds to $d_S = 100 \pm 44$ μm (mean ± s.d., $n = 100000$ pairwise distances). The log-likelihoods of these two models are comparable (–2467 vs. −2466), which does not allow for model selection or rejection on the basis of the observed data. However, the Euclidean distance model has a considerably smaller log-likelihood (–2502) than the other two models suggesting that a metric based on surface and graph distance describes the weak interactions better.

Discussion

Analyzing the patterns of dividing NSCs in adult zebrafish brains with a probabilistic model, we observe a preference for the positive influence model with a rather large interaction radius of 100 μm or 6 neighboring cells, respectively. The weak influence strength of 1.15 and 1.17, respectively, (a strength of $g = 1$ corresponds to random patterns) fits to the visual impression that S-phase NSCs are neither strongly clustered, nor particularly regular spaced on the zebrafish hemispheres. Our approach quantifies this impression, by taking the heterogeneous distribution of NSCs into account. Random spatial distributions of cells entering cell cycle have been observed in other systems, such as the ear epidermis (27,28). Individual stochastic cellular behavior resulting in a controlled

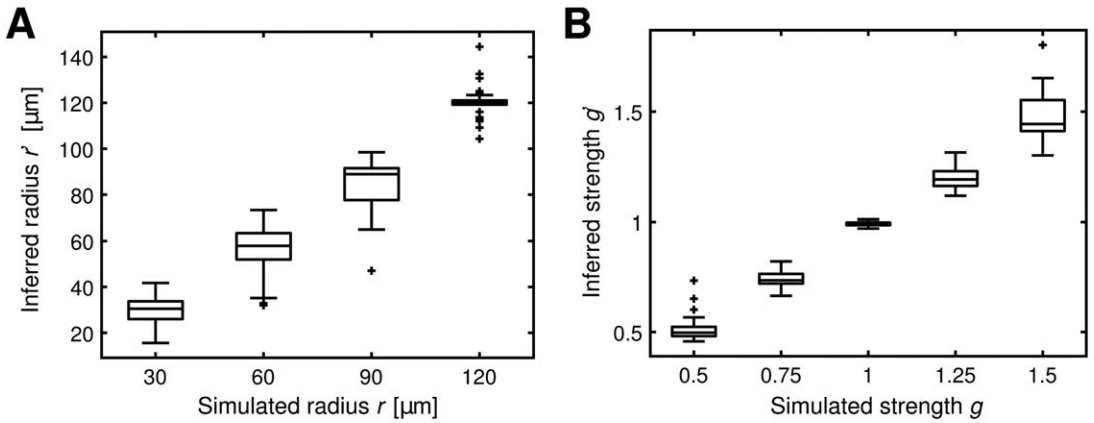

Figure 6. Model inference on simulated data works for a variety of radii r based on the surface distance d_S (**A**) and strengths g (**B**). For each parameter set, we simulated 30 spatial pattern on each of the six hemisphere and find the maximum likelihood estimate [Eq. (3)]. Box boundaries indicate the 25th and 75th percentile, respectively, the black line within the box marks the median. Whiskers above and below the box include points that are not outliers.

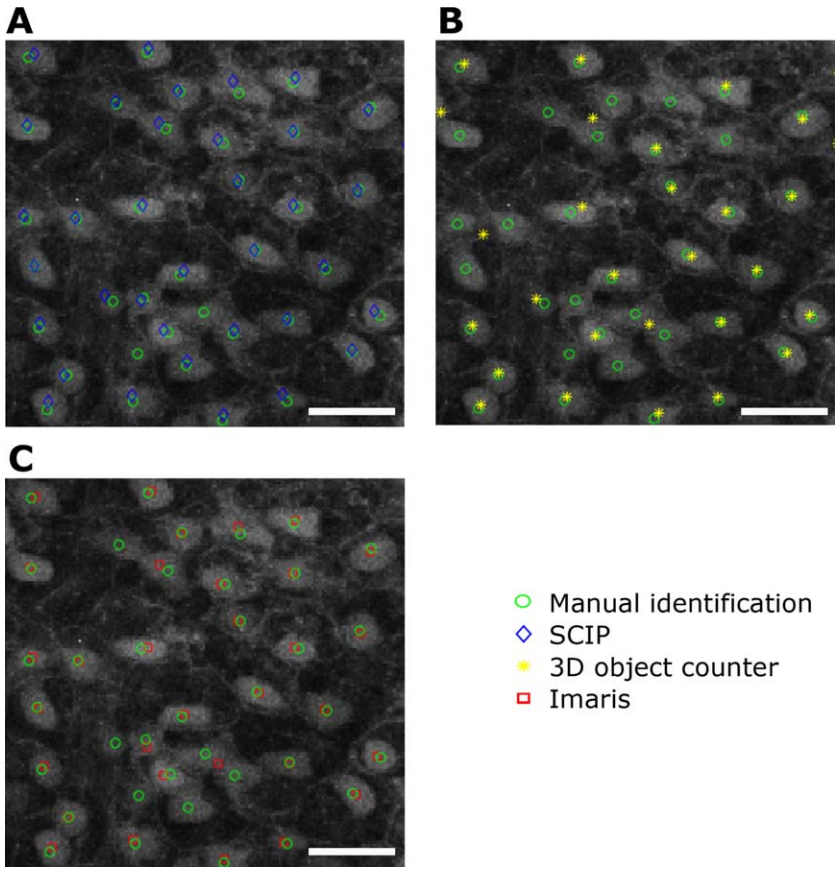

Figure 7. Evaluation of SCIP. We use manually (by P.C.) identified NSCs in different image regions on the 2D maximum intensity projection as ground truth (green circles). We evaluate SCIP (**A**), the 3D object counter plugin in ImageJ (**B**), and Imaris (**C**) by comparison of the identified cells to the manually detected ones. Scale bar: 30 μm. [Color figure can be viewed at wileyonlinelibrary.com]

growth of organs has been also observed in the retina (29), in the intestinal crypts (30), or in Arabidopsis sepals (31). The emergence of tissue with regular size and organization from unpredictable individual cell behavior, therefore, seems to be a robust strategy for tissue maintenance. However, the mechanisms regulating the amount of cycling NSCs have to be further investigated. Based on our present analysis, we detect randomness, but we cannot reject more complicated models with, for example, a large heterogeneity in cell cycle times, or a spatiotemporal dependence of NSCs entering cell cycle.

Our single-cell identification pipeline concatenates existing bioimage informatics processing steps and implicitly fits a 2D surface. While for the present study we compared our approach only to two other basic cell identification methods, recently proposed approaches could help identify single cells in challenging in vivo setting [see e.g., Arteta et al. (32) or Cireşan et al. (33)]. In the future, we would like to extend our approach to the segmentation of single cells, supplemented by a morphological analysis that might also allow for functional predictions (34). It would be interesting to see if cells in S-Phase can be inferred from the morphology of the GFP signal alone, and how strong cell positions correlate with morphological features.

A more detailed analysis would require a spatiotemporal analysis of division patterns also with other spatial statistics methods like Ripley's K (35) or the pair correlation function (36) to test the existence of between-timepoint influence. Overall it will be important in the future to decipher the mechanisms of synchronization of stem cells activity, to understand how groups of cells coordinate their recruitment. In this regard, comparing patterns between young and old animals might help to understand the mechanisms of stem cell depletion during aging.

Table 3. Parameter inference on 6 hemispheres finds a weak positive influence between S-phase NSCs for all three models with surface, graph, and Euclidean distance

MODEL METRIC	RADIUS (r)	STRENGTH (g)	LOG-LIKELIHOOD
Graph distance (d_G)	6 (cells)	1.17	−2466
Surface distance (d_s)	100 (μm)	1.15	−2467
Euclidean distance (d_E)	89 (μm)	1.16	−2502

Acknowledgments

The authors thank Michael Strasser, Carolin Loos, Dennis Rickert and the rest of the QSCD group for helpful comments. Also they thank Jovica Ninkovic and Tamara Durovic for software support.

Author Contributions

V.L. developed the pipeline with F.B. and performed analyses. P.C. performed all experiments. V.L. and C.M. wrote the article with P.C. C.M. and P.C. conceived and supervised the study.

Literature Cited

1. Clark PJ, Evans FC. Distance to nearest neighbor as a measure of spatial relationships in populations. Ecology 1954;35:445–453.
2. Tarnita CE, Bonachela JA, Sheffer E, Guyton JA, Coverdale TC, Long RA, Pringle RM. A theoretical foundation for multi-scale regular vegetation patterns. Nature 2017;541:398–401.
3. Krige DG. A statistical approach to some basic mine valuation problems on the Witwatersrand. J South Afr Inst Min Metall 1951;52:119–139.
4. Watanabe M, Kondo S. Is pigment patterning in fish skin determined by the Turing mechanism? Trends Genet 2015;31:88–96.
5. Chapouton P, Jagasia R, Bally-Cuif L. Adult neurogenesis in non-mammalian vertebrates. Bioessays 2007;29:745–757.
6. Bond AM, Ming G-L, Song H. Adult mammalian neural stem cells and neurogenesis: Five decades later. Cell Stem Cell 2015;17:385–395.
7. Mueller T, Wullimann MF. An evolutionary interpretation of teleostean forebrain anatomy. Brain Behav Evol 2009;74:30–42.
8. März M, Chapouton P, Diotel N, Vaillant C, Hesl B, Takamiya M, Lam CS, Kah O, Bally-Cuif L, Strähle U. Heterogeneity in progenitor cell subtypes in the ventricular zone of the zebrafish adult telencephalon. Glia 2010;58:870–888.
9. Than-Trong E, Bally-Cuif L. Radial glia and neural progenitors in the adult zebrafish central nervous system. Glia 2015;63:1406–1428.
10. Barbosa JS, Sanchez-Gonzalez R, Di Giaimo R, Baumgart EV, Theis FJ, Götz M, Ninkovic J. Neurodevelopment. Live imaging of adult neural stem cell behavior in the intact and injured zebrafish brain. Science 2015;348:789–793.
11. Dray N, Bedu S, Vuillemin N, Alunni A, Coolen M, Krecsmarik M, Supatto W, Beaurepaire E, Bally-Cuif L. Large-scale live imaging of adult neural stem cells in their endogenous niche. Development 2015;142:3592–3600.
12. Chinta R, Wasser M. Three-dimensional segmentation of nuclei and mitotic chromosomes for the study of cell divisions in live Drosophila embryos. Cytometry Part A 2012;81A:52–64.
13. Wählby C, Sintorn I-M, Erlandsson F, Borgefors G, Bengtsson E. Combining intensity, edge and shape information for 2D and 3D segmentation of cell nuclei in tissue sections. J Microsc 2004;215:67–76.
14. Al-Kofahi Y, Lassoued W, Lee W, Roysam B. Improved automatic detection and segmentation of cell nuclei in histopathology images. IEEE Trans Biomed Eng 2010;57:841–852.
15. Mathew B, Schmitz A, Muñoz-Descalzo S, Ansari N, Pampaloni F, Stelzer EHK, Fischer SC. Robust and automated three-dimensional segmentation of densely packed cell nuclei in different biological specimens with Lines-of-Sight decomposition. BMC Bioinf 2015;16:187.
16. Faure E, Savy T, Rizzi B, Melani C, Stašová O, Fabrèges D, Špir R, Hammons M, Čúnderlík R, Recher G, et al. A workflow to process 3D+time microscopy images of developing organisms and reconstruct their cell lineage. Nat Commun 2016;7:8674.
17. Schmitz A, Fischer SC, Mattheyer C, Pampaloni F, Stelzer EHK. Multiscale image analysis reveals structural heterogeneity of the cell microenvironment in homotypic spheroids. Sci Rep 2017;7:43693.
18. Schmitz C, Eastwood BS, Tappan SJ, Glaser JR, Peterson DA, Hof PR. Current automated 3D cell detection methods are not a suitable replacement for manual stereologic cell counting. Front Neuroanat 2014;8:27.
19. Bernardos RL, Raymond PA. GFAP transgenic zebrafish. Gene Express Patterns 2006;6:1007–1013.
20. Delaunay B. Sur la sphere vide. Izv. Akad. Nauk SSSR, Otdelenie Matematicheskii i Estestvennyka Nauk. 1934;7:1–2.
21. Floyd RW. Algorithm 97: Shortest path. Commun ACM 1962;5:345.
22. Warshall S. A Theorem on Boolean matrices. J ACM 1962;9:11–12.
23. Lever J, Krzywinski M, Altman N. Points of significance: Classification evaluation. Nat Methods 2016;13:603–604.
24. Bolte S, Cordelières FP. A guided tour into subcellular colocalization analysis in light microscopy. J Microsc 2006;224:213–232.
25. Schneider CA, Rasband WS, Eliceiri KW. NIH Image to ImageJ: 25 years of image analysis. Nat Methods 2012;9:671–675.
26. Chapouton P, Skupien P, Hesl B, Coolen M, Moore JC, Madelaine R, Kremmer E, Faus-Kessler T, Blader P, Lawson ND, et al. Notch activity levels control the balance between quiescence and recruitment of adult neural stem cells. J Neurosci 2010;30:7961–7974.
27. Doupé DP, Klein AM, Simons BD, Jones PH. The ordered architecture of murine ear epidermis is maintained by progenitor cells with random fate. Dev Cell 2010;18:317–323.
28. Mesa KR, Kawaguchi K, Gonzalez DG, Cockburn K, Boucher J, Xin T, Klein AM, Greco V. Epidermal stem cells self-renew upon neighboring differentiation. 2017. Available at: https://doi.org/10.1101/155408
29. He J, Zhang G, Almeida AD, Cayouette M, Simons BD, Harris WA. How variable clones build an invariant retina. Neuron 2012;75:786–798.
30. Snippert HJ, van der Flier LG, Sato T, van Es JH, van den Born M, Kroon-Veenboer C, Barker N, Klein AM, van Rheenen J, Simons BD, et al. Intestinal crypt homeostasis results from neutral competition between symmetrically dividing Lgr5 stem cells. Cell 2010;143:134–144.
31. Hong L, Dumond M, Tsugawa S, Sapala A, Routier-Kierzkowska A-L, Zhou Y, Chen C, Kiss A, Zhu M, Hamant O, et al. Variable cell growth yields reproducible organ development through spatiotemporal averaging. Dev Cell 2016;38:15–32.
32. Arteta C, Lempitsky V, Noble JA, Zisserman A. Learning to detect cells using non-overlapping extremal regions. In: Ayache N, Delingette H, Golland P, Mori K, editors. Medical Image Computing and Computer-Assisted Intervention – MICCAI 2012. Vol 7510. Lecture Notes in Computer Science. Berlin, Heidelberg: Springer Berlin Heidelberg; 2012. pp 348–356.
33. Cireşan DC, Giusti A, Gambardella LM, Schmidhuber J. Mitosis detection in breast cancer histology images with deep neural networks. Med Image Comput Comput Assist Interv 2013;16:411–418.
34. Buggenthin F, Buettner F, Hoppe PS, Endele M, Kroiss M, Strasser M, Schwarzfischer M, Loeffler D, Kokkaliaris KD, Hilsenbeck O, et al. Prospective identification of hematopoietic lineage choice by deep learning. Nat Methods 2017;14:403–406.
35. Ripley BD. Modelling spatial patterns. J R Stat Soc Series B Stat Methodol 1977;39:172–212.
36. Wiegand T, Moloney KA. Handbook of Spatial Point-Pattern Analysis in Ecology. Boca Raton, Florida: CRC Press; 2013. 538 p.